THE JOURNAL OF PHYSICAL CHEMISTRY LETTERS
A JOURNAL OF THE AMERICAN CHEMICAL SOCIETY

pubs.acs.org/JPCL Letter

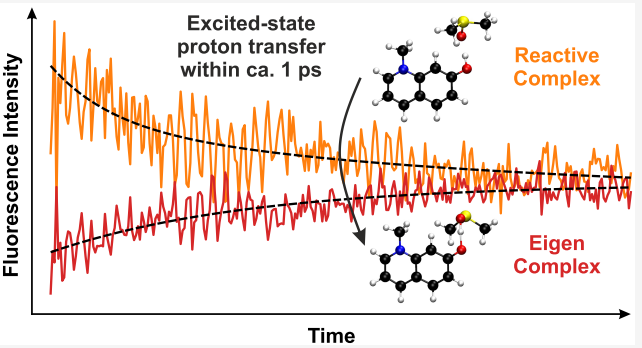
Molecular Dynamics of the Ultrafast Excited-State Proton Transfer of the Super-Photoacid NM7HQ$^+$ to the Aprotic Solvent DMSO

Niklas Sülzner,* Rafael Souza Mattos, and Mario Barbatti*

Cite This: J. Phys. Chem. Lett. 2025, 16, 9124−9134 Read Online

ACCESS | Metrics & More | Article Recommendations | Supporting Information

ABSTRACT: Photoacids exhibit an increase in acidity upon electronic excitation, providing powerful tools for studying excited-state proton transfer (ESPT) reactions. While these photoacids have been used extensively in experiments, theoretical studies, particularly on the dynamics, are largely lacking. Here, we report on the ultrafast ESPT of the super-photoacid *N*-methyl-7-hydroxyquinolium (NM7HQ$^+$) to the aprotic solvent DMSO, studied using excited-state ab initio molecular dynamics (AIMD). We combine TDDFT with the implicit solvent model PCM to simulate 400 trajectories for 3 ps, starting in the S_1 state. Our simulations reveal a short-lived equilibrium between the initially excited photoacid−DMSO complex (CPX) and the so-called Eigen complex (EC), the ESPT product, established within 1 ps. Subsequently, the EC undergoes a slow separation via a rotational motion on the ps time scale, further driving the ESPT. These results imply that the ESPT within the CPX may be significantly faster (<1 ps) than previously expected (2−3 ps).



Downloaded via RUHR UNIVERSITAT BOCHUM on August 27, 2025 at 08:07:12 (UTC).
See https://pubs.acs.org/sharingguidelines for options on how to legitimately share published articles.

Proton transfer in both the electronic ground and electronically excited states is of fundamental importance in chemistry and related fields.[1−3] Examples are countless and omnipresent, ranging from acid−base catalysis[4] and proton membranes in fuel cells,[5] to diverse biochemical mechanisms,[6,7] such as proton transfer in electronically excited states of various biological chromophores.[8−10] In this context, photoacids, i.e., compounds that undergo an acidity increase upon electronic excitation, play a central role. Prototypical examples of photoacids are the neutral hydroxy (OH) and cationic ammonium (NH_3^+) aromatic compounds.[11,12] Apart from various applications including photocatalysis,[13] bioimaging,[14] and single-molecule microscopy[15] (e.g., see ref 11 for a recent review), these photoacids have been established as powerful tools for probing excited-state proton transfer (ESPT) reactions by offering a precise time control, e.g., when using pulsed lasers.

The ESPT of photoacids has been extensively studied with respect to different environments, spectroscopic techniques, and theory (as recently reviewed in ref 12). For example, ESPT in aqueous solution has been demonstrated to follow an Eigen-Weller model:[16−18]

$$\mathrm{AH}^* + \mathrm{B} \overset{(1)}{\rightleftharpoons} \underbrace{[\mathrm{AH}^*\cdot\mathrm{B}]}_{\mathrm{CPX}} \overset{(2)}{\rightleftharpoons} \underbrace{[\mathrm{A}^{-*}\cdot\mathrm{HB}^+]}_{\mathrm{HBIP}} \overset{(3)}{\rightleftharpoons} \underbrace{[\mathrm{A}^{-*}\cdots\mathrm{HB}^+]}_{\mathrm{SSIP}} \overset{(4)}{\rightleftharpoons} \underbrace{\mathrm{A}^{-*} + \mathrm{HB}^+}_{\mathrm{FIP}} \quad (1)$$

In its most general form, this model involves four steps and five photoacid species, accounting for: (1) The formation of a reactive encounter complex ([AH* · B], CPX) via diffusion of the free excited photoacid (AH*) and the proton-accepting base (B); (2) the fast proton transfer within the CPX under the formation of a (hydrogen-bonded) contact-ion pair ([A$^-$ · HB$^+$], CIP/HBIP); (3) the stepwise diffusive separation of the HBIP into various solvent-separated ion pairs ([A$^-$ ··· HB$^+$], SSIP); and (4) the final separation into the fully separated (or free) ion pair (A^{-*}/HB$^+$, FIP). Only step (2) is easily accessible in molecular dynamics (MD) simulations due to computational limitations regarding the other diffusive steps.

The photoacid strength as quantified by pK_a^* (i.e., pK_a in the excited state; usually S_1) is decisive for the ESPT characteristics in different environments. While weak and moderately strong photoacids (pK_a^* > 0) are sufficient for ESPT in water due to effective proton stabilization via hydrogen bonding (HB), nonaqueous solutions, particularly aprotic solvents, require much stronger super-photoacids (with pK_a^* < 0).[12,19] One of these super-photoacids established for the study of nonaqueous ESPT is *N*-methyl-7-hydroxyquinolinium (NM7HQ$^+$; see Figure 1), characterized by pK_a = 5.9 and pK_a^* = −2.3.[20] This photoacid was first introduced by Kim and Topp,[21] who revived the original idea of Bardez et al.[22] of

Received: July 17, 2025
Revised: August 15, 2025
Accepted: August 21, 2025

ACS Publications © XXXX American Chemical Society

https://doi.org/10.1021/acs.jpclett.5c02202
J. Phys. Chem. Lett. 2025, 16, 9124−9134

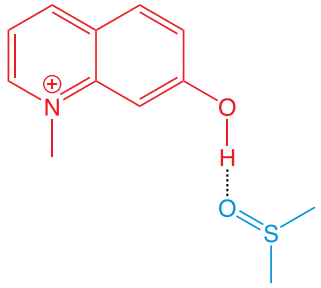


Figure 1. Molecular structure of the complex (CPX) between the super-photoacid $NM7HQ^+$ (in red) and the aprotic solvent DMSO (in blue), corresponding to the global minimum conformer.

blocking the photobasic nitrogen site in quinolines with a methyl (CH_3) group. Not only does this methylation switch off the competing photobasicity, it also enhances the photoacidity compared to the parent 7-hydroxyquinoline (7HQ; pK_a = 8.7, pK_a^* = 0.4).[23] Both 7HQ[24−32] and $NM7HQ^+$[20,33−43] have received extensive, ongoing attention by the group of Kwon, with a special focus on the role of hydrogen bonding and hydrogen-bonded solvent chains in the ESPT. The ESPT in hydrogen-bonded complexes of $NM7HQ^+$ with alcohols,[20,34,35] dimethyl sulfoxide (DMSO),[34,41,42] and *N*-methylbenzamide[40] in acetonitrile solution as well as in diols[36] has been investigated.

Owing to its positive charge in the nondissociated form, $NM7HQ^+$ represents a special type of a photoacid (cf. note 44). Since the corresponding base (A) of a positively charged photoacid (AH^+) is charge neutral, the proton transfer (step 2, eq 1) within CPX does not yield an HBIP, but a so-called Eigen complex (EC) of the form $[A^* \cdot HB^+]$ instead. Therefore, the ESPT mechanism of such a super-photoacid in aprotic solvents is effectively terminated at step 3 in the ESPT mechanism (eq 1). However, this termination step has only been recently successfully studied for the first time by Kwon and co-workers, at the example of $NM7HQ^+$ in DMSO−acetonitrile mixtures.[41,42] First, they found a 1:1 hydrogen-bonded CPX between $NM7HQ^+$ and DMSO as a prerequisite for the ESPT to yield the EC as a transient intermediate. The general importance of such an EC as a short-lived, rarely observed ESPT intermediate has been recently discussed in ref 45. Second, they demonstrated the subsequent separation of the EC under the involvement of a second DMSO molecule into a Zundel-like cation $[(DMSO)_2 \cdot H^+]$. Focusing on the EC formation upon collisional ESPT (on the ns time scale), the authors omitted the contribution from ESPT after direct excitation of pre-existing CPX, as they monitored the slower dynamics and paid less attention to the ultrashort time scale. Resolving the ultrafast dynamics of the initial proton transfer (ca. 2−3 ps) is experimentally harder due to finite time resolutions (typically a few 100 fs), but falls into the regime feasible for molecular dynamics simulations.

Existing studies on the ESPT mechanism have predominantly focused on the PT step, partially due to the challenging conditions of protic solvents, especially water (e.g., short lifetimes of the intermediates), but also intentionally as part of a race among superphotoacids toward increasingly fast ESPT. Simkovitch et al. proposed a division of the existing set of photoacids into four regimes according to their pK_a^* and suggested a theoretical solvent-controlled limit for the ESPT rate of 10^{13} s^{-1} (100 fs).[46] While ESPT rates in protic solvents are (due to higher proton conductivities) significantly higher compared to aprotic ones, the latter provide simpler environments that lack extensive HB networks (due to their missing HB donation), overall enhancing the lifetime of the ESPT intermediates. Thus, using a super-photoacid in an aprotic solvent is an ideal environment for selectively probing the initial PT in the ESPT mechanism (step 2 in eq 1).

In contrast to the wealth of experimental studies, theoretical studies on the ESPT—particularly regarding the dynamics and using simulation techniques—are still scarce, mostly focusing on the much faster intramolecular ESPT (ESIPT) reactions.[47−49] Importantly, studying the actual dynamics of the ESPT—as an excited-state reaction—requires *ab initio* molecular dynamics (AIMD) techniques for electronically excited states, which also allow for changes in the electronic state, i.e., nonadiabatic effects.[50] The most used technique for nonadiabatic dynamics is the surface-hopping approach,[51] which has been applied to study ESIPT.[52] To the best of our knowledge, no nonadiabatic studies have been reported on intermolecular ESPT (only adiabatic ones[53−64]), nor on ESPT in nonaqueous solutions

In this work, we study the ultrafast intermolecular ESPT of the super-photoacid $NM7HQ^+$ to the aprotic solvent DMSO (Figure 1) using AIMD simulations in the S_1 excited state. We apply time-dependent density functional theory (TDDFT; ωB97X-D) for the electronic structure and the polarizable continuum model (PCM) for implicit solvation. The system is given the possibility to relax into the S_0 ground state via surface hopping, but no hops are observed, effectively showcasing the adiabatic dynamics in S_1. This particular combination of photoacid and base has been chosen because it is the smallest example of ESPT in a nonaqueous solution for which direct experimental reference data are available. Thereby, we provide additional information on the mechanistic details of the ESPT in a nonaqueous solution, representing one of the few AIMD studies on intermolecular ESPT.

PRELIMINARY STATIC CALCULATIONS

At the S_0 equilibrium structure of the $NM7HQ^+$−DMSO complex (referred to as **CPX**), the strongest UV/vis absorption at 4.1 eV can be assigned to a transition into the bright S_1 state with $\pi \rightarrow \pi^*$ character (see Figure 2). Due to usage of the equilibrium conditions for PCM (i.e., using the refractive index instead of the dielectric constant) when treating excited states, the corresponding emission energy at the same S_0 structure (with the solvent equilibrated to S_0) is 4.0 eV with the solvent equilibrated to S_1. From this Franck−Condon (**FC**) point, the structure relaxes into the S_1 equilibrium with an emission energy of 3.6 eV. A significant contribution to this Stokes shift is the contraction (13 pm) of the HB to DMSO, in parallel to a slight elongation (5 pm) of the O−H bond in $NM7HQ^+$, constituting an overall strengthening of the HB. The ESPT in the **CPX** proceeds via a transition state (**TS**) with an (electronic) activation energy of ca. 3 kJ mol^{-1}, in which the proton is almost symmetrically shared between the donor (122 pm) and acceptor (118 pm) oxygen atoms at the photoacid and $NM7HQ^+$, respectively. At an overall energetic cost in the same order of magnitude (ca. 2 kJ mol^{-1}), the product of the ESPT, i.e., the so-called Eigen complex (**EC**) is formed, in which the proton resides at the acceptor site of the DMSO (106 pm) with a significantly larger distance to the donor O of the photoacid (143 pm). It should be noted that the emission energies of the **TS** (3.4 eV) and the **EC** (3.3 eV) are very

https://doi.org/10.1021/acs.jpclett.5c02202
J. Phys. Chem. Lett. 2025, 16, 9124−9134

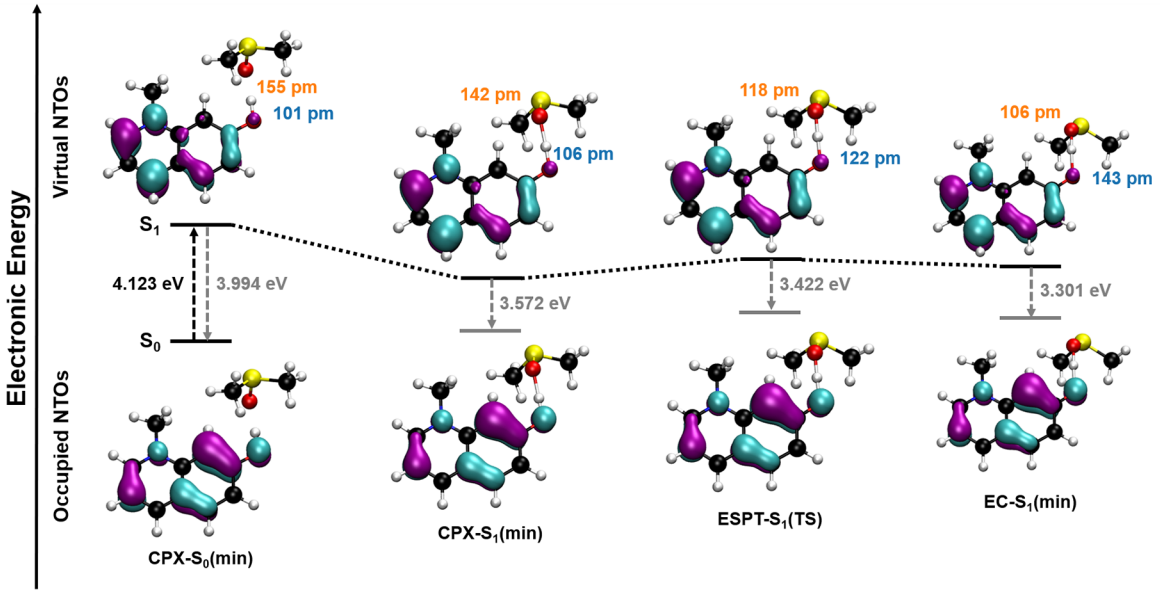


Figure 2. Reaction path for the ESPT from $NM7HQ^+$ to DMSO. Optimized structures for the S_0 and S_1 minima of **CPX**, the ESPT transition state (**TS**), and the S_1 minimum of **EC** (i.e., after ESPT) are shown. The energies for the initial $S_0 \rightarrow S_1$ absorption (in black) and $S_1 \rightarrow S_0$ emission (in gray) are given. O−H distances for the donating photoacid (in blue) and accepting DMSO (in orange) are included. The occupied and virtual parts of the dominant NTO pairs are shown in the bottom and top structures, respectively.

similar and that the character of the S_1 remains the same in **CPX**, **TS**, and **EC** (cf. Table S1; Supporting Information). Only after a complete separation (i.e., at an infinite distance), the emission of the free base species reaches a value of 3.1 eV, with an O−H distance of 96 pm in the protonated DMSO, additionally ca. 30 kJ mol^{-1} lower in energy compared to the **EC**.

CPX and therefore also **TS** and **EC** exhibit conformational flexibility concerning the orientation of the OH group and the HB orientation of the DMSO molecule, yielding in total eight main conformers each (see Table S2). The structure studied here (cf. Figures 1 and 2) refers to the global minimum (see Tables S3 and S4), but its activation and reaction energy for the ESPT are largest among the conformers (see Table S5). However, no significant effect on the ESPT dynamics is expected due to the large excess energy of ca. 0.5 eV that is provided during the relaxation from **FC** on S_1. This value amounts to approximately eight times the ESPT activation energy of each conformer, rendering the ESPT quasi-barrierless. Thus, the AIMD simulations have been performed on this single conformer.

While the level of theory applied here systematically overestimates the absolute absorption and emission energies by ca. 0.7−0.8 eV compared to the experimental band maxima (see Table 1), the relative energy differences (e.g., Stokes shifts) are reproduced reasonably well with deviations of only 0.1−0.2 eV. In particular, the experimental shift between **CPX** (2.83 eV) and **EC** (2.58 eV) emission of 0.25 eV, which controls the thermodynamics of the ESPT, is nicely reproduced by the calculations (ca. 0.27 eV), providing evidence for the validity of this level of theory. Also the energy difference between the excited acid (ROH^+*) and conjugated base (RO*) suggests an acidity jump $\Delta pK_a^* = pK_a^* - pK_a$ upon excitation of −8.2 based on the Förster cycle (see Figure S1 and its discussion in the Supporting Information),[67] in perfect agreement with the experimental value.[20] Moreover, the fluorescence lifetimes calculated based on the spontaneous emission rate (cf. eq 2) are in fair agreement with the experimental ones. Second-order wave function-based methods like ADC(2) or CC2 combined with PCM get closer to the experimental band maxima, but as post-HF methods their combination with an implicit solvent model raises the known issue of selecting an appropriate coupling scheme for the self-consistent reaction field (SCRF) procedure to include solvent effects beyond the HF level (see Table S6 and its discussion in the Supporting Information),[68] in addition to their significantly higher computational costs. At all relevant configurations (i.e., **CPX**, **TS**, and **EC**) in S_1, S_1 is separated by at least 1 eV from S_2 and higher states, with S_2 being significantly less bright (cf. Table S7). Besides, errors due to the small basis-set size or absence of diffuse functions were found to be not an issue (cf. Table S6). Thus, this TDA-TDDFT level of theory is considered satisfactory for the AIMD simulations, starting in the S_1 state.

Table 1. Comparison of the Calculated and Experimental characteristic properties, i.e., Absorption and Emission Energies [in eV (nm)] and Emission Lifetimes (in ns) of the Different Chemical Species in DMSO

	Absorption		Emission		Lifetime	
	Calc.[a]	Exptl.[b]	Calc.[a]	Exptl.[b]	Calc.[a]	Exptl.[b]
ROH^+	4.350	3.54	3.815	2.88	4.3	9.12[c]
	(285)	(350)	(325)	(430)	—	~6.8−7.5[d]
RO	3.631	2.75	3.086	2.34	7.3	6.5
	(341)	(450)	(402)	(530)	—	—
CPX	4.123	3.30	3.572	2.83	5.4	n.a.
	(301)	(375)	(347)	(438)	—	—
EC	n.a.	n.a.	3.301	2.58	5.1	n.a.
	(n.a.)	(n.a.)	(376)	(480)	—	—

[a]PCM-RI-TDA-TDDFT(ωB97X-D)/def2-SVP. [b]Taken from refs41, 42. [c]In acetonitrile (MeCN). [d]Value in DMSO estimated from that in MeCN using $\tau \propto n^{-p}$ (p = 2,3)[65] with the refractive indices n (DMSO: 1.479; MeCN:1.344).[66]

https://doi.org/10.1021/acs.jpclett.5c02202
J. Phys. Chem. Lett. 2025, 16, 9124−9134

FOLLOWING THE ESPT IN TIME

To monitor the progress of the ESPT, i.e., following the position of the transferred proton in time, different structural descriptors have been tested: (i) the O−H distance $d_{OH}^{(X)} = |r_H - r_X|$ from the photoacid donor (X = D) or DMSO acceptor (X = A); (ii) a proton-transfer coordinate $\delta = (d_{OH}^{(A)} - d_{OH}^{(D)}) \cdot |r_D - r_A|^{-1}$ as frequently used in ground-state PT studies[69,70] and (iii) the O−H displacement $\Delta d_{OH}^{(X)} = d_{OH}^{(X)} - d_{OH}^{(X)}(eq)$ relative to its value at the optimized S_1(min) structure of **CPX**. The following discussion is mostly restricted to (ii), i.e., the PT coordinate, as this appears most useful to us. However, it is not as intuitive as the simple O−H distance (i). Still, alternative versions of all main plots using the other variables can be found in the Supporting Information.

The typical time evolution of the PT coordinate of a single trajectory is shown as the thin (red) line in Figure 3(a). Two

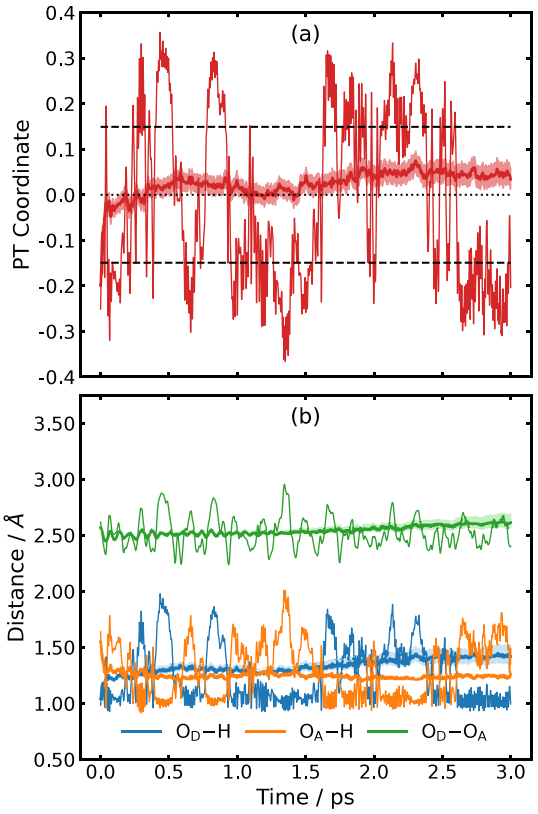


Figure 3. Time evolution of the proton-transfer (PT) coordinate δ (red), the O−H distances for the donor (blue) and acceptor (orange), and the donor−acceptor O−O distance (green) for a single trajectory (thin lines) and the ensemble average (thick lines) with the bootstrap confidence interval (95%) as uncertainty estimate (areas). Black dashed lines (in a) indicate the minimum and maximum values from the optimized geometries (cf. Figure 2) at ca. $\delta = \pm 0.15$ for reference.

chemical states can be identified: The proton can either reside at the photoacid (state **I**: $\delta \sim -0.15$) or at the DMSO (state **II**: $\delta \sim +0.15$). A value of $\delta = 0$ would indicate that the proton is symmetrically shared between the donor and acceptor atoms. For both states (**I** and **II**), the values for the PT coordinate from a single trajectory seem to be, on average, slightly larger than the limiting values suggested by the optimized S_1 structures. A similar trend is observed in the O−H distance (cf. Figure 3(b) and Figure S2): The O−H distance matches well for the photoacid (ca. 1 Å), but is somewhat larger for DMSO (ca. 1.5 Å) in the nontransferred state (**II**). Another important feature of the behavior observed here is the highly dynamic character, i.e., the proton is constantly being transferred between the donor and acceptor in a single-trajectory picture.

Averaged over all trajectories, the evolution of the PT coordinate changes to a picture represented by the thick (red) line in Figure 3(a). Directly after excitation, the PT coordinate first undergoes an ultrafast (ca. 10 fs) increase from ca. −0.2 (i.e., smaller than at S_1(min)) to ca. −0.1, mostly due to relaxation from the Franck−Condon point on the S_1 surface toward its minimum. Subsequently, the PT coordinate further increases, peaking at a positive value around 0.5 ps. Between 0.5 and 1.5 ps, the value decreases to zero before it continues to rise again, reaching a plateau after 3.0 ps. Although a value of $\delta \sim 0$ would indicate a symmetrically shared proton (i.e., a structure close to the transition state), the regions near zero should be better understood as the average between 50% of trajectories that are in state **I** and 50% that are in state **II**, giving rise to a zero mean value. Thus, the changes resulting from effective ESPT are, on average, rather subtle. We describe the changes shortly after excitation up to ca. 1.5 ps to the ESPT, converting the **CPX** into the **EC**, and those between 1.5 and 3.0 ps to a subsequent separation step, effectively further draining the **EC** population.

A comparative look at the O−H distances shows that the O−H acceptor distance is almost constant, whereas the donor distance continues to increase (cf. Figure 3(b)). Moreover, a significant difference regarding the variability as quantified by the standard deviations (SDs) can be observed (cf. Figure S2). While the SD of the O−H distance remains mostly constant for DMSO, it starts to significantly increase for the photoacid after 1.5 ps (Figure S2(b)). This behavior could be traced back to some trajectories (see Figure S3) in which a roaming between the deprotonated photoacid and the protonated DMSO occurred after ESPT. However, the same trend persists even if these trajectories are excluded from the averaging (see Figure S2(c)), showing that this behavior is only partially due to the roaming. We suspected an intermolecular translational-rotational motion as the origin of this behavior. To further investigate this, we calculated the distance and relative orientation between the photoacid and DMSO (excluding the transferred proton), defined in terms of the center-of-mass (COM) distances and an angle between the normal vector of the best-fitting ring plane and the direction vector of the S−O bond, respectively. As can be seen in Figures S4 and S5, the distance between the centers changes only slowly (ca. 0.2 Å), while the relative orientation changes drastically (>10°), especially after 1.5 ps. Altogether, these results indicate that the changes after 1.5 ps are predominantly due to an intramolecular rotation rather than a translation within the **EC**.

Besides, the O−H distance for DMSO shows an oscillation (up to 1 ps) with a period of ca. 60−70 fs, corresponding to 475−550 cm^{-1}, which is also visible in the donor−acceptor O−O distance (green plots in Figure 3(b)). This frequency range covers several ring skeletal modes with the O_D and O_A approaching (see Table S8), particularly the deformation modes at 537 cm^{-1} and 557 cm^{-1} of **CPX-S_1(eq)**, which may assist the ESPT by lowering the effective energy barrier.

https://doi.org/10.1021/acs.jpclett.5c02202
J. Phys. Chem. Lett. 2025, 16, 9124−9134

CORRELATING THE ENERGY GAP WITH THE PROTON DISTANCE

Having demonstrated the usefulness of the PT coordinate for describing the different protonation states during the ESPT, we can now use it to replace the time coordinate, which leads to insightful correlations with the S_1-S_0 energy gap (see Figure 4 and Figure S6). This is particularly interesting as the S_1-S_0 energy gap depends on the current protonation state.

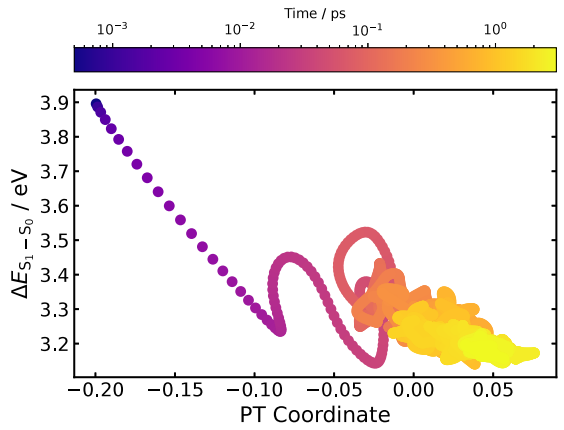


Figure 4. S_1-S_0 energy gap $\Delta E_{S_1-S_0}$ (in eV) as a function of the PT coordinate δ for the ensemble average. Time information is encoded by color, using a logarithmic scale, as indicated by the color bar.

Figure 4 shows the mean S_1-S_0 energy gap plotted against the mean PT coordinate (averaged over all trajectories). This representation replaces time with the PT coordinate, providing a clear view of how the S_1-S_0 energy gap evolves along the reaction path. In this way, the horizontal axis acts as an effective reaction coordinate, similar to a potential energy profile, but derived from our ensemble dynamics. A rapid decrease of the energy gap from ca. 3.9 eV (at $\delta = -0.2$) to ca. 3.2 eV (at $\delta = -0.1$) occurs within the first 20 fs. Then, the energy gap reveals an apparent barrier, increasing to a value of approximately 3.45 eV, while decreasing to a value of $\delta \sim -0.075$. Having passed the barrier, the energy gap drops to a value of <3.2 eV (at $\delta = -0.025$) after 40 fs. From here on, the energy gap first increases to a value of ca. 3.5 eV, with the PT coordinate changing only slightly, and then becomes highly flexible. After these 100 fs, the energy gap decays from 3.4 eV (at $\delta = -0.025$) to an apparent asymptotic value of 3.15 eV at the largest value of the PT coordinate of ca. $\delta = -0.05$. Interestingly, this clear initial progression is only observed in the ensemble average, but not in the individual trajectories, which is why we refer to it as a collective motion. The logarithmic color scale that decodes the time information (cf. Figure 4) reveals a persistence of ca. 100 fs.

The value of 3.9 eV is close to the emission energy at the Franck−Condon point directly after excitation (4.0 eV), whereas values of 3.5−3.6 eV and 3.2−3.3 eV are characteristic of **CPX** and **EC** near their S_1 minima, respectively. The simulation of the absorption and emission spectra from the initial conditions using the nuclear ensemble approach[71] reveals that the band maxima are approximately 0.1 eV lower than the vertical excitation energies (cf. Figure S7). In line with the previous discussion, we thus attribute the initial decay to the relaxation from the Franck−Condon point in combination with ultrafast ESPT within 50−100 fs, yielding the **EC**. Moreover, we ascribe the less pronounced changes between 0.1 and 1.0 ps to an equilibration between **CPX** and **EC**, explained as follows: Despite the effective barrier in $\Delta E_{S_1-S_0}$, a ballistic proton transfer takes place in most of the trajectories during the relaxation from FC due to the excessive kinetic energy, allowing it to almost instantaneously cross the barrier. As an endothermic process (ΔE = +3 kJ mol^{-1}), the system can equilibrate from this nonequilibrium situation after the ESPT, converting some of the **EC** back into **CPX**. Additionally, **CPX** that has not initially reacted can perform an ESPT, yielding **EC** on the slower 0.1−1.0 ps time scale. A simple Stokes−Einstein estimate for bulk translational diffusion in DMSO yields times of several picoseconds for Å-scale displacements, which is much slower than our subpicosecond ESPT, confirming that the process is not diffusion-limited. The even slower dynamics on the 1.0−3.0 ps time scale describe a subsequent effective separation of the **EC**. The corresponding whole-body rotational time from the Stokes−Einstein-Debye relation is in the many-picosecond range, indicating that the 1−3 ps motion observed here is an internal reorientation within the complex rather than bulk rotational diffusion.

EXCITED-STATE DECAY KINETICS

For the closest possible comparison with the available experimental time-resolved fluorescence data by Kwon and co-workers,[42] we aimed to model the temporal decay of fluorescence intensity. In the first step, we calculated the populations of the different chemical species by applying energy windows (see Figure 5). These allow for counting the populations based on the current value of the energy gap of each trajectory at a given time. To reduce the statistical noise, this counting is achieved in time bins of 10 fs, i.e., the check is performed in these bins and the counts are summed up. The corresponding populations of the different species are shown in Figure 5(a−b).

The unrelaxed **CPX** (**CPX-FC**, in blue) is only present at time zero and disappears extremely fast, as expected. Surprisingly, the relaxed **CPX** (**CPX-Eq**, in orange) and the **EC** (in green) appear to have similar populations at the beginning. Whereas the population of **CPX-Eq** continuously decays to roughly half its initial value over the range of 3 ps, that of **EC** exhibits a weakly pronounced biphasic behavior with an initial rise within 1 ps and a subsequent slow decay. With the smallest energy gap, the population of a further separated species (**EC-Sep**, in red) experiences a continuous increase over the full range of 3 ps, approaching ca. triple of its initial value of 2.5. As also demonstrated in Figure 5(a), both the sum of the populations of all species as well as the partial sum of **CPX** and **EC** are reasonably constant, in line with proper counting. Interestingly, the initial decay of **CPX(FC)** does not yield a rise of **CPX-Eq**, but rather **EC** and **EC-Sep**, pointing toward a direct ESPT during the relaxation.

Having the populations at hand, we calculated the fluorescence intensities. For this, we did not simply sum the counts in the time bins but instead weighted the counts by the spontaneous emission rate at the individual times (as opposed to weighting by 1, as for the populations).[72] The spontaneous emission rate for the $S_1 \rightarrow S_0$ transition is given by

$$\Gamma_{1\rightarrow 0} = \frac{2\alpha}{\hbar m_e c^2} \Delta E_{1\rightarrow 0}^2 f_{1\rightarrow 0} \quad (2)$$

https://doi.org/10.1021/acs.jpclett.5c02202
J. Phys. Chem. Lett. 2025, 16, 9124−9134

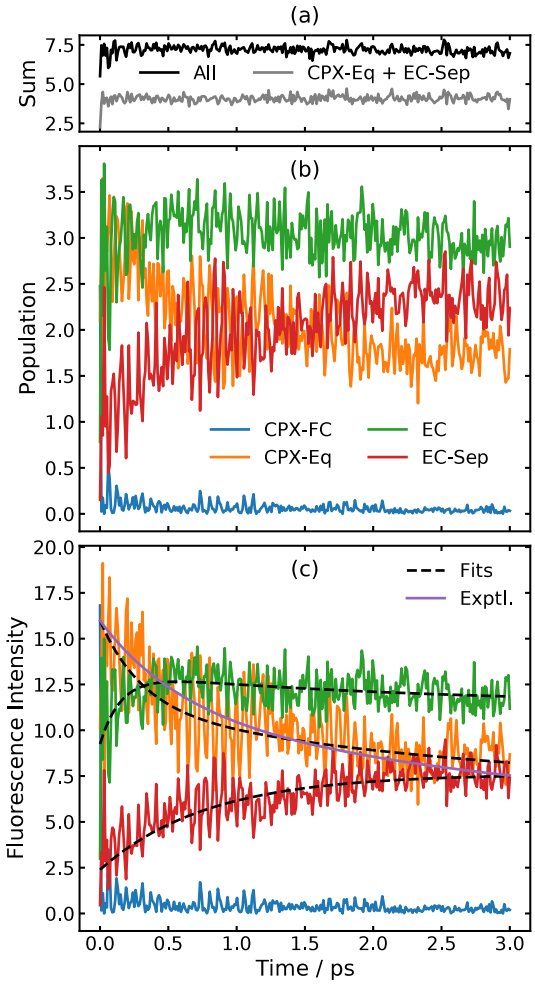


Figure 5. Time evolution of the sum (a) and individual populations (b), as well as the simulated fluorescence intensity (c) of the different chemical species defined based on energy windows. Each window is centered at a given value [CPX-Eq (3.90 eV), CPX-FC (3.47 eV), EC (3.20 eV), EC-Sep (3.00 eV)] and includes a width of ± 0.05 eV. The triexponential decay reported by Kwon and co-workers is included as experimental reference.[42] Dashed lines indicate multiexponential fits to the different decays (cf. Table 2).

with $\Delta E_{1\to 0}$ and $f_{1\to 0}$ as, respectively, the energy and oscillator strength of the transition, and some natural constants (α: fine-structure constant; $\hbar$: reduced Planck constant; m_e: electron mass; c: speed of light). The corresponding time evolution of the simulated fluorescence intensity is shown in Figure 5(c). Validation of the assignment of the chemical species based on the energy gap is further given by the correlation with the structural data (cf. Figure S8), revealing a nice clustering of the data points.

Qualitatively, the fluorescence intensity follows the same trends as the populations. The key message remains the same: **CPX** is effectively converting into **EC** and **EC-Sep**. In analogy to what is done experimentally, we fitted the temporal fluorescence decays of **CPX-Eq**, **EC**, and **EC-Sep** to multi-exponential functions

$$I(t) = \sum_{i=0}^{N} A_i \exp(-t/\tau_i) = \sum_{i=0}^{N} A_i \exp(-k_i t) \tag{3}$$

with the amplitudes $\{A_i\}$ and lifetimes $\{\tau_i\}$ (or rate constants $\{k_i\}$) as parameters. The fits are determined by minimizing

$$\chi^2 = \sum_{j=1}^{n} \left(\frac{I_j^{(\mathrm{obs})} - I_j^{(\mathrm{fit})}}{\sigma_j} \right)^2 = \sum_{j=1}^{n} \left(\frac{r_j}{\sigma_j} \right)^2 \tag{4}$$

i.e., the sum of the residuals $r_j = I_j^{(\mathrm{obs})} - I_j^{(\mathrm{fit})}$ (as the differences between the observed and modeled fluorescence intensities) divided by the standard deviations of the error σ_j (taken from the ensemble averaging) for all n time bins. Due to its biphasic behavior, a biexponential fit ($N = 2$) is necessary for **EC**, while a monoexponential fit ($N = 1$) is sufficient for **EC-Sep**. In the case of **CPX-Eq**, both mono- and biexponential fits were performed. The optimized parameters are listed in Table 2.

Table 2. Results of the Fits of the Simulated Fluorescence Decay to Multiexponential Functions (cf. Eq. 3)

	A_0[a]	A_1	τ_1	A_2	τ_2	χ^2
CPX-Eq	8.412	6.564	711	—	—	2.120
CPX-Eq	6.649	4.597	305	4.734	2810	2.091
EC	12.247	−4.412	782	—	—	1.053
EC	11.414	−3.905	155	1.741	2146	1.036
EC-Sep	7.609	−5.222	782	—	—	2.232

[a]Constant offset (i.e., $\tau_0 \to \infty$)

CPX-Eq shows a slightly better agreement for a biexponential (χ^2 = 2.09) than a monoexponential (χ^2 = 2.12) fit, revealing contributions with similar amplitudes from a faster (ca. 0.3 ps) and a slower (ca. 3 ps) contribution. In particular, the fast component is in fair agreement with the rise time (0.1−0.2 ps) of the **EC** signal from a biexponential fit. The **EC** decay is found to be ca. 2 ps, which is comparable to that for the **CPX-Eq**. Restricting to the monoexponential fits that capture the average lifetimes, the rise time of the **EC-Sep** signal (ca. 1 ps) matches well the decay time of **CPX(eq)**, providing evidence for their mechanistic relation. However, the decay of **EC** does not match the rise of **EC-Sep**, as would be expected in the case of a sequential conversion, which may appear counterintuitive. We ascribe this paradox to a difference in the time scales and the establishment of chemical equilibrium in the excited state: After approximately 0.5 ps, the population and thus the signal of **EC** become constant, as an equilibrium between **CPX-Eq** and **EC** has been established due to the ESPT. Subsequently, i.e., from 1 ps on, the **EC** turns into **EC-Sep** due to the intramolecular rotation that separates the zwitterion of $NM7HQ^+$ from the protonated DMSO. Thus, effective conversion of **CPX-Eq** into **EC-Sep** is observed on the longer time scale—with the (monoexponential) decay of **CPX-Eq** matching the rise of **EC-Sep**—and a roughly constant **EC** population.

COMPARISON WITH THE PREVIOUS EXPERIMENTS

This interpretation is in agreement with the experimental results by Kwon and co-workers.[42] They reported a triexponential decay of the **CPX-Eq** signal (monitored at 450 nm) with fitted amplitudes 0.39, 0.48, and 0.36 and lifetimes 0.6, 4, and 110 ps, respectively. The first two were assigned to the ESPT of a *pre-equilibrium* (PE) between **CPX-Eq** and **EC**, while the slowest represents the **EC** decay. Their experimental fit (purple line in Figure 5(c)) is in fair agreement with our biexponential fit to the simulated **CPX-Eq** decay. It should be noted that the slowest component (110 ps) is beyond the reach of our simulations, as it behaves quasi-constant up to the

https://doi.org/10.1021/acs.jpclett.5c02202
J. Phys. Chem. Lett. 2025, 16, 9124−9134

maximum simulation time of 3 ps. Moreover, Kwon and coworkers used only the first two fast components to calculate an amplitude-weighted lifetime (AWL) according to

$$\tau_{ave}^{(Kwon)} = \frac{A_1\tau_1 + A_2\tau_2}{A_1 + A_2} \quad (5)$$

of 2.6 ps (i.e., 2−3 ps), describing the ESPT from the PE state. However, since their fit is triexponential, we rather propose using a *fractional* AWL based on the full AWL

$$\tau_{ave} = \frac{\sum_{i=1}^{N=3} A_i\tau_i}{\sum_{i=1}^{N=3} A_i} = \sum_{i=1}^{N=3} \frac{A_i}{\sum_{j=1}^{N=3} A_j}\tau_i = \sum_{i=1}^{N=3} f_i\tau_i \quad (6)$$

by truncating the summation at $N = 2$. Thereby, $\tau_{ave}^{(1,2)} = f_1\tau_1 + f_2\tau_2 = 1.75$ ps includes all amplitudes in the denominator of the weighting factors f_i. Such a fractional AWL has the important advantage that it adds up together with the remaining weighted lifetimes to the full AWL according to eq 6, e.g., $\tau_{ave} = \tau_{ave}^{(1,2)} + f_3\tau_3$, in contrast to the AWL in eq 5. The value of $\tau_{ave}^{(1,2)}$ is slightly smaller than that of $\tau_{ave}^{(Kwon)}$, in overall better agreement with our simulations (e.g., the monoexponential fit). Still, we suggest not referring to these AWLs, but the pure lifetimes from the fits instead. As can be seen, both the fast (0.3 ps (sim.) vs 0.6 ps (exptl.)) and the intermediate (2 ps (sim.) vs 4 ps (exptl.)) components of the **CPX-Eq** decay are in good agreement between experiment and simulation.

While a time scale of 300 fs may appear relatively short for ESPT, approaching that of ESIPT (e.g., 50 fs for 3-hydroxyflavone),[64] similar ESPT lifetimes have been reported for other hydrogen-bonded systems. In general, such ultrafast ESPT requires either a particularly strong photoacid or Brønsted base. Very recently, Verma et al. reported ESPT of 4-hydroxychalcone ($pK_a^* \sim 0$) to 1-methyl-imidazole or *tert*-butyl amine within 500 fs,[73] which is comparable to that of $NM7HQ^+$ ($pK_a^* \sim -2$) to DMSO studied here. Similarly, Grandjean et al. observed sub-ps ESPT for a hydroxypyrene-based super-photoacid ($pK_a^* \sim -3$) to trioctylphosphine oxide (TOPO).[74] Heo et al. found a coherent ESPT within 60 fs for the related parent photoacid HPTS (8-hydroxypyrene-1,3,6-trisulfonate) ($pK_a^* \sim 1$) to acetate as a much stronger base.[61] Interestingly, they found a 246 cm^{-1} ring vibration that assists with the ESPT within the first 30−40 fs. Lastly, the ESPT of quinone cyanine 9 (QCy9), which is one of the strongest photoacids available ($pK_a^* \sim -8$), is known to take place within 50 fs in water.[75]

According to the division of photoacids based on their pK_a^* by Simkovitch et al.,[46] $NM7HQ^+$ falls into category II ($-4 < pK_a^* < 0$), for which the ESPT is still mainly limited by the basicity of the solvent, but possible in protic solvents other than water (compared to category I: $pK_a^* > 0$). For the stronger photoacids from category III ($pK_a^* \sim -6$), the ESPT rate constant, k_{PT}, is limited by the orientational relaxation of the solvent as described by the solvation correlation function $S(t)$. Horng et al. reported solvation dynamics (derived from multiexponential fit of $S(t)$) for DMSO on three time scales: 214 fs, 2.29 ps, and 10.7 ps.[76] A comparison between this short-time component (214 fs) and the time scale of 300 fs observed here suggests that the ESPT of $NM7HQ^+$ to DMSO is close to being controlled by the solvation dynamics (i.e., category III). Moreover, the good agreement between the intermediate-time component (2.29 ps) and the 2−3 ps time scale for **EC** separation is in line with its interpretation as rotational diffusion.

In summary, this work applies *ab initio* molecular dynamics (AIMD) using surface hopping to study the ultrafast dynamics of the excited-state proton transfer (ESPT) of the super-photoacid $NM7HQ^+$ to the aprotic solvent DMSO. The simulations confirm a rapid equilibration between the photoacid−DMSO complex, **CPX**, and the so-called Eigen complex, **EC**, that is formed upon ESPT. Challenging previous assumptions, the ESPT is ultrafast (<1 ps) and does not take place on a slower time scale of 2−3 ps, as deduced from experiments. Subsequently, the **EC** experiences a slow separation via a rotational motion (>1 ps), even though no explicit solvent (i.e., directional specific interactions) is accounted for; as would be expected in reality. Interestingly, this finding bears a vague resemblance to the diffusive separation of the **EC** under the involvement of a second DMSO molecule into a Zundel-like cation, as observed in the experiments. Overall, this study provides additional information on the mechanistic details of the ESPT of superphotoacids in a nonaqueous solution.

As the main limitation of our approach, we identify the usage of a dielectric continuum solvent model. Due to their purely electrostatic nature, these models do not account for specific solvent−solute interactions, which are assumed to be most responsible for discrepancies compared to the experiment. Particularly, the encapsulation of the molecules within the solvent cavity causes an artificial binding that prevents complete separation (e.g., via diffusion). Thus, for future work, going beyond implicit solvation, e.g., by using mixed quantum-mechanical/molecular-mechanical (QM/MM) approaches, appears necessary for a better description of the local solvation (e.g., as done in ref 63.). Such accurate, yet efficient approaches become even more important when studying larger systems like the related hydroxypyrene superphotoacids.[77−80]

COMPUTATIONAL METHODS

Static Calculations. Before the AIMD simulations, we performed static quantum-chemical calculations to explore the reaction path for the ESPT reaction between $NM7HQ^+$ and DMSO. For this, we selected density functional theory (DFT) and time-dependent DFT (TDDFT)[81] with the long-range-separated, dispersion-corrected ωB97X-D functional[82,83] and the def2-SVP basis[84,85] set in combination with the conductor-like polarizable continuum model (C-PCM; in short: PCM)[86,87] for implicit solvation in DMSO ($\epsilon_r = 46.45$, $n = 1.479$)[66] as our target level of theory. The ORCA program (version 5.0.3)[88,89] was used due to the availability of PCM-TDDFT excited-state gradients,[90] employing the resolution-of-the-identity (RI) approximation (RIJONX)[91,92] and the Tamm-Dancoff approximation (TDA)[93] for TDDFT excitation energies. In addition, we exemplarily tested this level of theory against higher-level coupled-cluster methods and basis-set effects using TURBOMOLE (version 7.8).[94,95] For the best comparison between the solvent models in ORCA and TURBOMOLE, the PCM parameters in ORCA were chosen to reproduce the TDDFT results obtained with the related conductor-like screening model (COSMO)[96,97] in TURBOMOLE (see Supporting Information for further details).

UV/vis absorption energies were calculated as (vertical) ($S_0 \rightarrow S_{n>0}$) excitation energies at equilibrium structures in the S_0 ground state (PCM nonequilibrium conditions), while

https://doi.org/10.1021/acs.jpclett.5c02202
J. Phys. Chem. Lett. 2025, 16, 9124−9134

fluorescence emission energies were calculated as ($S_1 \rightarrow S_0$) de-excitation energy at the S_1 equilibrium structure (PCM equilibrium conditions). S_1 structure optimizations invoked a total number of two excited states. The guess for the transition between the S_1 equilibrium structures before and after ESPT was taken from the minimum energy path obtained using the nudged elastic band climbing-image (NEB-CI) method. Different PCM conditions are necessary to properly incorporate solvation effects on the excited state in the case of absorption and fluorescence energies, respectively. With PCM-TDDFT, a distinction regarding the choice of the dielectric constant is made to reflect the different time scales of the (fast) electronic and (slow) solvent redistribution.[87] While the solvent contributions to the ground state are evaluated using the actual dielectric constant of the medium (ϵ_r), those for an excited state in nonequilibrium solvation are evaluated using the *optical* dielectric constant (n^2, with the refractive index n), reflecting that the solvent distribution has not yet adjusted to the excited state, as in the case of absorption. In contrast, under equilibrium conditions, the real dielectric constant of the medium is used for long-lived excited states to describe equilibrium solvation, as required for fluorescence. However, the solvent charges are not explicitly equilibrated with S_1 under these equilibrium conditions, as this would require more sophisticated state-specific (SS) approaches.[87]

AIMD Simulations. *Ab initio* nonadiabatic molecular dynamics simulations were performed using the Newton-X NS program (version 3.5.2)[98] with the fewest switches surface hopping (FSSH) algorithm,[51] combined with ORCA (version 6.0.1)[88,89] for the electronic structure. At the level mentioned above, i.e., PCM-RI-TDA-TDDFT(ωB97X-D)/def2-SVP, we simulated the dynamics of the structure (single conformer) shown in Figure 1 in an implicit solution of 400 trajectories, each for 3 ps and with a 0.5 fs time step, starting in the S_1 state. The time-dependent Baeck-An (TD-BA) approximation[99] was employed, approximating the nonadiabatic couplings as a function of the energy gaps and their second time derivatives. The use of surface hopping gives the system the possibility to switch into the S_0 ground state. However, no hops are observed in this study, and thus, the dynamics are effectively adiabatic. Initial conditions (1000) for the positions and velocities were generated from a quantum-harmonic oscillator Wigner distribution[71,100,101] based on the (harmonic) frequencies and normal modes of the $NM7HQ^+$−DMSO dimer at the S_0 equilibrium structure, using Nexton-X CS (version 2.6 (build 01, 2023−10−25)).[98,102] Hereby, both low- and high-frequency modes associated with the CH_3 groups in both $NM7HQ^+$ and DMSO were kept frozen, as suggested by Janoš et al.[103] Of these 1000 initial conditions, the 400 for trajectories were selected from the corresponding absorption spectrum with a center at 4.0 eV and an energy window of ± 0.2 eV. Importantly, the parameter thresholds in ORCA for the DFT integration grids needed to be tightened to `defgrid-3` for a stable propagation with sufficient energy conservation.

■ ASSOCIATED CONTENT

Supporting Information

The Supporting Information is available free of charge at https://pubs.acs.org/doi/10.1021/acs.jpclett.5c02202.

> Determination of the acidity jump ΔpK_a^* using the Förster cycle at TDA-TDDFT; Benchmarking different levels of theory for the vertical excitation energies; Natural transition orbitals and vertical transition energies for the first two excitations; Investigation of the conformational flexibility; Assignment of selected characteristic vibrational modes; Time evolution of O−H distance, PT coordinate, and O−H displacements (Ensemble average; EA); Time evolution of O−H displacement, ring−SO angle, and ring−SO distance (Individual trajectories; IT); Energy gap as a function of the O−H distance, PT coordinate, and O−H displacement (EA); UV/vis absorption and fluorescence emission spectra simulated with nuclear ensemble approaches; Correlation of the simulated fluorescence intensity (EA); Time evolution of ring−SO angle, ring−SO distance (geometry center and center-of-mass), and ring atom RMSD (IT, EA) (PDF)

■ AUTHOR INFORMATION

Corresponding Authors

Niklas Sülzner − *Aix Marseille University, CNRS, ICR, Marseille 13397, France; Lehrstuhl für Theoretische Chemie, Ruhr-Universität Bochum, 44801 Bochum, Germany;* orcid.org/0000-0002-8734-5807; Email: niklas.suelzner@rub.de

Mario Barbatti − *Aix Marseille University, CNRS, ICR, Marseille 13397, France; Institut Universitaire de France, Paris 75231, France;* orcid.org/0000-0001-9336-6607; Email: mario.barbatti@univ-amu.fr

Author

Rafael Souza Mattos − *Aix Marseille University, CNRS, ICR, Marseille 13397, France;* orcid.org/0000-0003-0215-7100

Complete contact information is available at: https://pubs.acs.org/10.1021/acs.jpclett.5c02202

Notes

The authors declare no competing financial interest.

■ ACKNOWLEDGMENTS

N. S. thanks the Deutsche Forschungsgemeinschaft (DFG, German Research Foundation) for funding through project 388390466 (TRR 247) and under Germany's Excellence Strategy−EXC 2033−390677874−RESOLV. Computing resources have been provided by HPC@ZEMOS. R. S. M. and M. B. received support from the French government under the France 2030 investment plan as part of the Initiative d'Excellence d'Aix-Marseille Université (A*MIDEX AMX-22-IN1-48). They acknowledge the Centre de Calcul Intensif d'Aix-Marseille for granting access to its high-performance computing resources.

■ REFERENCES

(1) Chou, P.-T.; Solntsev, K. M. Photoinduced Proton Transfer in Chemistry and Biology. *J. Phys. Chem. B* **2015**, *119*, 2089−2089.
(2) Kagel, H.; Frohme, M.; Glökler, J. Photoacids in biochemical applications. *Journal of Cellular Biotechnology* **2019**, *4*, 23−30.
(3) Hammes-Schiffer, S. Virtual Issue on Proton Transfer. *J. Phys. Chem. B* **2021**, *125*, 3725−3726.
(4) Saway, J.; Salem, Z. M.; Badillo, J. J. Recent Advances in Photoacid Catalysis for Organic Synthesis. *Synthesis* **2021**, *53*, 489−497.

(5) Shabani, M.; Younesi, H.; Pontié, M.; Rahimpour, A.; Rahimnejad, M.; Zinatizadeh, A. A. A critical review on recent proton exchange membranes applied in microbial fuel cells for renewable energy recovery. *Journal of Cleaner Production* **2020**, *264*, 121446.
(6) Neupane, P.; Bhuju, S.; Thapa, N.; Bhattarai, H. K. ATP Synthase: Structure, Function and Inhibition. *Biomolecular Concepts* **2019**, *10*, 1−10.
(7) Ghosh, I.; Khan, S.; Banerjee, G.; Dziarski, A.; Vinyard, D. J.; Debus, R. J.; Brudvig, G. W. Insights into Proton-Transfer Pathways during Water Oxidation in Photosystem II. *J. Phys. Chem. B* **2019**, *123*, 8195−8202.
(8) Laptenok, S. P.; Conyard, J.; Page, P. C. B.; Chan, Y.; You, M.; Jaffrey, S. R.; Meech, S. R. Photoacid behaviour in a fluorinated green fluorescent protein chromophore: ultrafast formation of anion and zwitterion states. *Chemical Science* **2016**, *7*, 5747−5752.
(9) Chen, C.; Zhu, L.; Baranov, M. S.; Tang, L.; Baleeva, N. S.; Smirnov, A. Y.; Yampolsky, I. V.; Solntsev, K. M.; Fang, C. Photoinduced Proton Transfer of GFP-Inspired Fluorescent Superphotoacids: Principles and Design. *J. Phys. Chem. B* **2019**, *123*, 3804−3821.
(10) Snellenburg, J. J.; Laptenok, S. P.; DeSa, R. J.; Naumov, P.; Solntsev, K. M. Excited-State Dynamics of Oxyluciferin in Firefly Luciferase. *J. Am. Chem. Soc.* **2016**, *138*, 16252−16258.
(11) Yucknovsky, A.; Amdursky, N. Photoacids and Photobases: Applications in Functional Dynamic Systems. *Angew. Chem.* **2025**, *137*, e202422963.
(12) Sülzner, N.; Jung, G.; Nuernberger, P. A dual experimental−theoretical perspective on ESPT photoacids and their challenges ahead. *Chemical Science* **2025**, *16*, 1560−1596.
(13) Saway, J.; Pierre, A. F.; Badillo, J. J. Photoacid-catalyzed acetalization of carbonyls with alcohols. *Organic & Biomolecular Chemistry* **2022**, *20*, 6188−6192.
(14) Finkler, B.; Riemann, I.; Vester, M.; Grüter, A.; Stracke, F.; Jung, G. Monomolecular pyrenol-derivatives as multi-emissive probes for orthogonal reactivities. *Photochemical & Photobiological Sciences* **2016**, *15*, 1544−1557.
(15) Menges, J. A.; Clasen, A.; Jourdain, M.; Beckmann, J.; Hoffmann, C.; König, J.; Jung, G. Surface Preparation for Single-Molecule Chemistry. *Langmuir* **2019**, *35*, 2506−2516.
(16) Eigen, M.; Kruse, W.; Maass, G.; Demaeyer, L. Rate Constants of Protolytic Reactions in Aqueous Solution. *Progress in Reaction Kinetics and Mechanism* **1964**, *2*, 285.
(17) Weller, A. Fast Reactions of Excited Molecules. *Progress in Reaction Kinetics and Mechanism* **1961**, *1*, 187.
(18) Leiderman, P.; Genosar, L.; Huppert, D. Excited-State Proton Transfer: Indication of Three Steps in the Dissociation and Recombination Process. *J. Phys. Chem. A* **2005**, *109*, 5965−5977.
(19) Tolbert, L. M.; Solntsev, K. M. Excited-State Proton Transfer: From Constrained Systems to "Super" Photoacids to Superfast Proton Transfer. *Acc. Chem. Res.* **2002**, *35*, 19−27.
(20) Park, S.-Y.; Lee, Y. M.; Kwac, K.; Jung, Y.; Kwon, O.-H. Alcohol Dimer is Requisite to Form an Alkyl Oxonium Ion in the Proton Transfer of a Strong (Photo)Acid to Alcohol. *Chemistry − A European Journal* **2016**, *22*, 4340−4344.
(21) Kim, T. G.; Topp, M. R. Ultrafast Excited-State Deprotonation and Electron Transfer in Hydroxyquinoline Derivatives. *J. Phys. Chem. A* **2004**, *108*, 10060−10065.
(22) Bardez, E.; Devol, I.; Larrey, B.; Valeur, B. Excited-State Processes in 8-Hydroxyquinoline: Photoinduced Tautomerization and Solvation Effects. *J. Phys. Chem. B* **1997**, *101*, 7786−7793.
(23) Codescu, M.-A.; Weiß, M.; Brehm, M.; Kornilov, O.; Sebastiani, D.; Nibbering, E. T. J. Switching between Proton Vacancy and Excess Proton Transfer Pathways in the Reaction between 7-Hydroxyquinoline and Formate. *J. Phys. Chem. A* **2021**, *125*, 1845−1859.
(24) Franz, J.; Peyerimhoff, S. D.; Hanrath, M.; Kwon, O.-H.; Jang, D.-J. Ab Initio Study of the Electronic Spectrum of 7-Hydroxyquinoline. *Chem. Lett.* **2005**, *34*, 330−331.
(25) Park, H. J.; Kwon, O.-H.; Ah, C. S.; Jang, D.-J. Excited-State Tautomerization Dynamics of 7-Hydroxyquinoline in β-Cyclodextrin. *J. Phys. Chem. B* **2005**, *109*, 3938−3943.
(26) Kwon, O.-H.; Kim, T. G.; Lee, Y.-S.; Jang, D.-J. Biphasic Tautomerization Dynamics of Excited 7-Hydroxyquinoline in Reverse Micelles. *J. Phys. Chem. B* **2006**, *110*, 11997−12004.
(27) Kwon, O.-H.; Lee, Y.-S.; Yoo, B. K.; Jang, D.-J. Excited-State Triple Proton Transfer of 7-Hydroxyquinoline along a Hydrogen-Bonded Alcohol Chain: Vibrationally Assisted Proton Tunneling. *Angew. Chem.* **2006**, *118*, 429−433.
(28) Park, K.; Shin, K. J.; Kim, H. Excited-state reversible geminate recombination in two dimensions. *J. Chem. Phys.* **2009**, *131*, 154105.
(29) Park, S.-Y.; Kwon, O.-H.; Kim, T. G.; Jang, D.-J. Ground-State Proton Transfer of 7-Hydroxyquinoline Confined in Biologically Relevant Water Nanopools. *J. Phys. Chem. C* **2009**, *113*, 16110−16115.
(30) Park, S.-Y.; Lee, Y.-S.; Kwon, O.-H.; Jang, D.-J. Proton transport of water in acid−base reactions of 7-hydroxyquinoline. *Chem. Commun.* **2009**, *0*, 926−928.
(31) Park, S.-Y.; Kim, B.; Lee, Y.-S.; Kwon, O.-H.; Jang, D.-J. Triple proton transfer of excited 7-hydroxyquinoline along a hydrogen -bonded water chain in ethers: secondary solvent effect on the reaction rate. *Photochemical & Photobiological Sciences* **2009**, *8*, 1611−1617.
(32) Kim, Y.-J.; Kwon, O.-H. Proton diffusion dynamics along a diol as a proton-conducting wire in a photo-amphiprotic model system. *Phys. Chem. Chem. Phys.* **2016**, *18*, 32826−32839.
(33) Park, S.-Y.; Kwon, O.-H.; Lee, Y.-S.; Jang, D.-J. Triplet-State Acid−Base Reactions of 1-Methyl-7-oxyquinolinium in Water. *J. Phys. Chem. A* **2009**, *113*, 10589−10592.
(34) Lee, Y. M.; Park, S.-Y.; Kim, H.; Kim, T. G.; Kwon, O.-H. Photoinduced strong acid−weak base reactions in a polar aprotic solvent. *Methods and Applications in Fluorescence* **2016**, *4*, 024004.
(35) Park, S.-Y.; Kim, T. G.; Ajitha, M. J.; Kwac, K.; Lee, Y. M.; Kim, H.; Jung, Y.; Kwon, O.-H. The critical size of hydrogen-bonded alcohol clusters as effective Brønsted bases in solutions. *Phys. Chem. Chem. Phys.* **2016**, *18*, 24880−24889.
(36) Kim, Y.-J.; Rakshit, S.; Jin, G. Y.; Ghosh, P.; Lee, Y. M.; Park, W.-W.; Kim, Y. S.; Kwon, O.-H. Synergistic Configuration of Diols as Brønsted Bases. *Chemistry − A European Journal* **2017**, *23*, 17179−17185.
(37) Adhikari, A.; Park, J.-H.; Nho, H.-W.; Kwon, O.-H. Residence and diffusion of a dynamically prototropic hydration probe in AOT reverse micelles. *J. Mol. Liq.* **2020**, *320*, 114346.
(38) Nho, H.-W.; Park, J.-H.; Adhikari, A.; Kwon, O.-H. Acid−base reaction of a cationic hydration probe in vicinity of anionic interface of AOT reverse micelles. *J. Mol. Liq.* **2021**, *326*, 115270.
(39) Nho, H.-W.; Adhikari, A.; Kwon, O.-H. Ultrafast Excited-State Proton Transfer of a Cationic Superphotoacid in a Nanoscopic Water Pool. *J. Phys. Chem. B* **2022**, *126*, 1275−1283.
(40) Choi, Y.-J.; Kim, H.; Kwon, O.-H. Acid−base reaction of a super-photoacid with a cooperative amide hydrogen-bonded chain. *Bulletin of the Korean Chemical Society* **2022**, *43*, 501−507.
(41) Choi, Y.-J.; Nho, H.-W.; Kim, Y.-J.; Kwon, O.-H. Quantifying the Ground-State Hydrogen-Bond Formation of a Super-Photoacid by Inspecting Its Excited-State Dynamics. *ChemPhotoChem.* **2024**, *8*, e202300164.
(42) Lee, S.-H.; Choi, Y.-J.; Kim, Y.-J.; Kee, J.-M.; Kwon, O.-H. Capturing an Eigen complex in an acid-base reaction shows step-resolved molecularity. *Cell Reports Physical Science* **2024**, *5*, 102155.
(43) Lee, S.-W.; Kwon, O.-H. Lifetimes and Lifetime-Associated Spectra for Reversible Excited Two-State Reactions. *J. Phys. Chem. A* **2025**, *129*, 447−458.
(44) Note that $NM7HQ^+$ is not referred to as a *cationic* photoacid since this term is used in the literature only for photoacids with a positively charged acidic group (e.g., NH_3^+), independent of the total charge.
(45) Sülzner, N. New light on proton transfer: Spectral and kinetic signature of a transient Eigen complex. *Chem.* **2024**, *10*, 3276−3278.

https://doi.org/10.1021/acs.jpclett.5c02202
J. Phys. Chem. Lett. 2025, 16, 9124−9134

(46) Simkovitch, R.; Shomer, S.; Gepshtein, R.; Huppert, D. How Fast Can. a Proton-Transfer Reaction Be beyond the Solvent-Control Limit? *J. Phys. Chem. B* **2015**, *119*, 2253−2262.
(47) Xia, S.-H.; Xie, B.-B.; Fang, Q.; Cui, G.; Thiel, W. Excited-state intramolecular proton transfer to carbon atoms: nonadiabatic surface-hopping dynamics simulations. *Phys. Chem. Chem. Phys.* **2015**, *17*, 9687−9697.
(48) Guo, W.-W.; Liu, X.-Y.; Chen, W.-K.; Cui, G. Excited-state proton transfer in 4−2'-hydroxyphneylpyridine: full-dimensional surface-hopping dynamics simulations. *RSC Adv.* **2016**, *6*, 85574−85581.
(49) Jankowska, J.; Barbatti, M.; Sadlej, J.; Sobolewski, A. L. Tailoring the Schiff base photoswitching − a non-adiabatic molecular dynamics study of substituent effect on excited state proton transfer. *Phys. Chem. Chem. Phys.* **2017**, *19*, 5318−5325.
(50) Crespo-Otero, R.; Barbatti, M. Recent Advances and Perspectives on Nonadiabatic Mixed Quantum−Classical Dynamics. *Chem. Rev.* **2018**, *118*, 7026−7068.
(51) Tully, J. C. Molecular dynamics with electronic transitions. *J. Chem. Phys.* **1990**, *93*, 1061−1071.
(52) Toldo, J. M.; do Casal, M. T.; Ventura, E.; do Monte, S. A.; Barbatti, M. Surface hopping modeling of charge and energy transfer in active environments. *Phys. Chem. Chem. Phys.* **2023**, *25*, 8293−8316.
(53) Guglielmi, M.; Tavernelli, I.; Rothlisberger, U. On the proton transfer mechanism in ammonia-bridged 7-hydroxyquinoline: a TDDFT molecular dynamics study. *Phys. Chem. Chem. Phys.* **2009**, *11*, 4549−4555.
(54) Bekçioğlu, G.; Hoffmann, F.; Sebastiani, D. Solvation-Dependent Latency of Photoacid Dissociation and Transient IR Signatures of Protonation Dynamics. *J. Phys. Chem. A* **2015**, *119*, 9244−9251.
(55) Petrone, A.; Donati, G.; Caruso, P.; Rega, N. Understanding THz and IR Signals beneath Time-Resolved Fluorescence from Excited-State Ab Initio Dynamics. *J. Am. Chem. Soc.* **2014**, *136*, 14866−14874.
(56) Chiariello, M. G.; Rega, N. Exploring Nuclear Photorelaxation of Pyranine in Aqueous Solution: an Integrated Ab-Initio Molecular Dynamics and Time Resolved Vibrational Analysis Approach. *J. Phys. Chem. A* **2018**, *122*, 2884−2893.
(57) Chiariello, M. G.; Donati, G.; Raucci, U.; Perrella, F.; Rega, N. Structural Origin and Vibrational Fingerprints of the Ultrafast Excited State Proton Transfer of the Pyranine-Acetate Complex in Aqueous Solution. *J. Phys. Chem. B* **2021**, *125*, 10273−10281.
(58) Chiariello, M. G.; Donati, G.; Rega, N. Time-Resolved Vibrational Analysis of Excited State Ab Initio Molecular Dynamics to Understand Photorelaxation: The Case of the Pyranine Photoacid in Aqueous Solution. *J. Chem. Theory Comput.* **2020**, *16*, 6007−6013.
(59) Chiariello, M. G.; Raucci, U.; Donati, G.; Rega, N. Water-Mediated Excited State Proton Transfer of Pyranine−Acetate in Aqueous Solution: Vibrational Fingerprints from Ab Initio Molecular Dynamics. *J. Phys. Chem. A* **2021**, *125*, 3569−3578.
(60) Raucci, U.; Chiariello, M. G.; Rega, N. Modeling Excited-State Proton Transfer to Solvent: A Dynamics Study of a Super Photoacid with a Hybrid Implicit/Explicit Solvent Model. *J. Chem. Theory Comput.* **2020**, *16*, 7033−7043.
(61) Heo, W.; Uddin, N.; Park, J. W.; Rhee, Y. M.; Choi, C. H.; Joo, T. Coherent intermolecular proton transfer in the acid−base reaction of excited state pyranine. *Phys. Chem. Chem. Phys.* **2017**, *19*, 18243−18251.
(62) Thomaz, J. E.; Walker, A. R.; Van Wyck, S. J.; Meisner, J.; Martinez, T. J.; Fayer, M. D. Proton Transfer Dynamics in the Aprotic Proton Accepting Solvent 1-Methylimidazole. *J. Phys. Chem. B* **2020**, *124*, 7897−7908.
(63) Walker, A. R.; Wu, B.; Meisner, J.; Fayer, M. D.; Martínez, T. J. Proton Transfer from a Photoacid to a Water Wire: First Principles Simulations and Fast Fluorescence Spectroscopy. *J. Phys. Chem. B* **2021**, *125*, 12539−12551.
(64) Li, Y.; Siddique, F.; Aquino, A. J. A.; Lischka, H. Molecular Dynamics Simulation of the Excited-State Proton Transfer Mechanism in 3-Hydroxyflavone Using Explicit Hydration Models. *J. Phys. Chem. A* **2021**, *125*, 5765−5778.
(65) Olmsted, J. Effect of refractive index on molecular radiative lifetimes. *Chem. Phys. Lett.* **1976**, *38*, 287−292.
(66) Spies, C.; Finkler, B.; Acar, N.; Jung, G. Solvatochromism of pyranine-derived photoacids. *Phys. Chem. Chem. Phys.* **2013**, *15*, 19893.
(67) Pines, D.; Pines, E. Solvent Assisted Photoacidity. In *Hydrogen-Transfer Reactions*; Hynes, J. T., Klinman, J. P., Limbach, H.-H., Schowen, R. L., Eds.; John Wiley & Sons, Ltd, 2006; pp 377−415, Section: 12 _eprint: https://onlinelibrary.wiley.com/doi/pdf/10.1002/9783527611546.ch12.
(68) Karbalaei Khani, S.; Marefat Khah, A.; Hättig, C. Comparison of Reaction Field Schemes for Coupling Continuum Solvation Models with Wave Function Methods for Excitation Energies. *J. Chem. Theory Comput.* **2020**, *16*, 4554−4564.
(69) Marx, D. Proton Transfer 200 Years after von Grotthuss: Insights from Ab Initio Simulations. *ChemPhysChem* **2006**, *7*, 1848−1870.
(70) Marx, D. Proton Transfer 200 Years after von Grotthuss: Insights from Ab Initio Simulations. *ChemPhysChem* **2007**, *8*, 209−210.
(71) Crespo-Otero, R.; Barbatti, M. Spectrum simulation and decomposition with nuclear ensemble: formal derivation and application to benzene, furan and 2-phenylfuran. *Theor. Chem. Acc.* **2012**, *131*, 1237.
(72) Braun, G.; Borges, I.; Aquino, A. J. A.; Lischka, H.; Plasser, F.; do Monte, S. A.; Ventura, E.; Mukherjee, S.; Barbatti, M. Non-Kasha fluorescence of pyrene emerges from a dynamic equilibrium between excited states. *J. Chem. Phys.* **2022**, *157*, 154305.
(73) Verma, P.; Mathew, R.; Dhiman, N.; Mitra, P. K.; Lakshmanna, Y. A. Ultrafast excited-state dynamics of 4-hydroxychalcone: role of intramolecular charge transfer and photoacidity. *Phys. Chem. Chem. Phys.* **2025**, *27*, 7716−7727.
(74) Grandjean, A.; Pérez Lustres, J. L.; Jung, G. Solvent-Controlled Intermolecular Proton-Transfer Follows an Irreversible Eigen-Weller Model from fs to ns. *ChemPhotoChem.* **2021**, *5*, 1094−1105.
(75) Simkovitch, R.; Shomer, S.; Gepshtein, R.; Shabat, D.; Huppert, D. Excited-State Proton Transfer from Quinone-Cyanine 9 to Protic Polar-Solvent Mixtures. *J. Phys. Chem. A* **2014**, *118*, 1832−1840.
(76) Cichos, F.; Willert, A.; Rempel, U.; von Borczyskowski, C. Solvation Dynamics in Mixtures of Polar and Nonpolar Solvents. *J. Phys. Chem. A* **1997**, *101*, 8179−8185.
(77) Sülzner, N.; Geissler, B.; Grandjean, A.; Jung, G.; Nuernberger, P. Excited-State Proton Transfer Dynamics of a Super-Photoacid in Acetone-Water Mixtures. *ChemPhotoChem.* **2022**, *6*, e202200041.
(78) Knorr, J.; Sülzner, N.; Geissler, B.; Spies, C.; Grandjean, A.; Kutta, R. J.; Jung, G.; Nuernberger, P. Ultrafast transient absorption and solvation of a super-photoacid in acetoneous environments. *Photochemical & Photobiological Sciences* **2022**, *21*, 2179−2192.
(79) Sülzner, N.; Hättig, C. Theoretical Study on the Photoacidity of Hydroxypyrene Derivatives in DMSO Using ADC(2) and CC2. *J. Phys. Chem. A* **2022**, *126*, 5911−5923.
(80) Sülzner, N.; Hättig, C. Computational investigation of explicit solvent effects and specific interactions of hydroxypyrene photoacids in acetone, DMSO, and water. *Phys. Chem. Chem. Phys.* **2023**, *25*, 11130−11144.
(81) Petrenko, T.; Kossmann, S.; Neese, F. Efficient time-dependent density functional theory approximations for hybrid density functionals: Analytical gradients and parallelization. *J. Chem. Phys.* **2011**, *134*, 054116.
(82) Chai, J.-D.; Head-Gordon, M. Long-range corrected hybrid density functionals with damped atom−atom dispersion corrections. *Phys. Chem. Chem. Phys.* **2008**, *10*, 6615−6620.
(83) Grimme, S.; Antony, J.; Ehrlich, S.; Krieg, H. A consistent and accurate ab initio parametrization of density functional dispersion

https://doi.org/10.1021/acs.jpclett.5c02202
J. Phys. Chem. Lett. 2025, 16, 9124−9134

correction (DFT-D) for the 94 elements H-Pu. *J. Chem. Phys.* **2010**, *132*, 154104.
(84) Weigend, F.; Ahlrichs, R. Balanced basis sets of split valence, triple zeta valence and quadruple zeta valence quality for H to Rn: Design and assessment of accuracy. *Phys. Chem. Chem. Phys.* **2005**, *7*, 3297−3305.
(85) Weigend, F. Accurate Coulomb-fitting basis sets for H to Rn. *Phys. Chem. Chem. Phys.* **2006**, *8*, 1057−1065.
(86) Cossi, M.; Rega, N.; Scalmani, G.; Barone, V. Energies, structures, and electronic properties of molecules in solution with the C-PCM solvation model. *J. Comput. Chem.* **2003**, *24*, 669−681.
(87) Mennucci, B. Polarizable continuum model. *WIREs Computational Molecular Science* **2012**, *2*, 386−404.
(88) Neese, F. The ORCA program system. *WIRES Comput. Mol. Sci.* **2012**, *2*, 73−78.
(89) Neese, F. Software update: the ORCA program system, version 5.0. *WIRES Comput. Mol. Sci.* **2022**, *12*, e1606.
(90) Garcia-Rates, M.; Neese, F. Effect of the Solute Cavity on the Solvation Energy and its Derivatives within the Framework of the Gaussian Charge Scheme. *J. Comput. Chem.* **2020**, *41*, 922−939.
(91) Neese, F. An improvement of the resolution of the identity approximation for the formation of the Coulomb matrix. *J. Comput. Chem.* **2003**, *24*, 1740−1747.
(92) Neese, F.; Olbrich, G. Efficient use of the resolution of the identity approximation in time-dependent density functional calculations with hybrid density functionals. *Chem. Phys. Lett.* **2002**, *362*, 170−178.
(93) Hirata, S.; Head-Gordon, M. Time-dependent density functional theory within the Tamm−Dancoff approximation. *Chem. Phys. Lett.* **1999**, *314*, 291−299.
(94) *TURBOMOLE V7.8 2023*, a development of University of Karlsruhe and Forschungszentrum Karlsruhe GmbH, 1989−2007, TURBOMOLE GmbH, since2007; available from https://www.turbomole.org.
(95) Franzke, Y. J.; Holzer, C.; Andersen, J. H.; Begušić, T.; Bruder, F.; Coriani, S.; Della Sala, F.; Fabiano, E.; Fedotov, D. A.; Fürst, S.; et al. TURBOMOLE: Today and Tomorrow. *J. Chem. Theory Comput.* **2023**, *19*, 6859−6890.
(96) Schäfer, A.; Klamt, A.; Sattel, D.; Lohrenz, J. C. W.; Eckert, F. COSMO Implementation in TURBOMOLE: Extension of an efficient quantum chemical code towards liquid systems. *Phys. Chem. Chem. Phys.* **2000**, *2*, 2187−2193.
(97) Klamt, A. The COSMO and COSMO-RS solvation models. *WIREs Computational Molecular Science* **2018**, *8*, e1338.
(98) Barbatti, M.; Bondanza, M.; Crespo-Otero, R.; Demoulin, B.; Dral, P. O.; Granucci, G.; Kossoski, F.; Lischka, H.; Mennucci, B.; Mukherjee, S.; et al. Newton-X Platform: New Software Developments for Surface Hopping and Nuclear Ensembles. *J. Chem. Theory Comput.* **2022**, *18*, 6851−6865.
(99) T. do Casal, M.; Toldo, J. M.; Pinheiro Jr, M.; Barbatti, M. Fewest switches surface hopping with Baeck-An couplings [version 2; peer review: 3 approved]. *Open Research Europe* **2021**, *1*, 49.
(100) Hillery, M.; O'Connell, R. F.; Scully, M. O.; Wigner, E. P. Distribution functions in physics: Fundamentals. *Phys. Rep.* **1984**, *106*, 121−167.
(101) Case, W. B. Wigner functions and Weyl transforms for pedestrians. *American Journal of Physics* **2008**, *76*, 937−946.
(102) Barbatti, M.; Granucci, G.; Ruckenbauer, M.; Plasser, R.; Crespo-Otero, F.; Pittner, J.; Persico, M.; Lischka, H. *NEWTON-X: A package for Newtonian dynamics close to the crossing seam*, Version 2, 2016, www.newtonx.org.
(103) Janoš, J.; Slavíček, P.; Curchod, B. F. E. Selecting Initial Conditions for Trajectory-Based Nonadiabatic Simulations. *Acc. Chem. Res.* **2025**, *58*, 261−270.

https://doi.org/10.1021/acs.jpclett.5c02202
J. Phys. Chem. Lett. 2025, 16, 9124−9134